Compressive properties of parametrically optimised mechanical metamaterials based on 3D projections of 4D geometries

Gabrielis Cerniauskas[a], Parvez Alam[a,*]

[a]*School of Engineering, The University of Edinburgh, Edinburgh, UK*

Abstract

The design process of 3D mechanical metamaterials is still an emerging field and in this paper, we propose for the first time, a new design and optimisation approach based on 3D projections of 4D geometries (4-polytopes) and evolutionary algorithms. We find that through iterative parametric optimisation, 4-polytope projected mechanical metamaterials can be optimised to achieve both high specific stiffness and high specific yield strengths. Samples manufactured using a low-stereolithography method were tested in compression. We find that optimised tesseracts (8-cell structures) had a higher specific yield strength (22.8 kNm/kg) than that of honeycomb structures tested out-of-plane (19.4 kNm/kg) and a specific stiffness of (0.68 MNm/kg) which is more than 3-fold that of gyroid structures. The compressive strength to solid-modulus ratio of the 8-cell tesseract is very high (3×10^{-3}), exceeding that of out-of-plane honeycombs, which are themselves closer in value to 5-cell pentatopes (2×10^{-3}). 8-cell and 5-cell structures are in the region of one order of magnitude higher than 16-cell and 24-cell structures ($\sim 2\times10^{-4} - 8\times10^{-4}$) and are hence comparable to nanostructured metamaterials. The 8-cell tesseracts are 18% stiffer, 43% stronger, and 19% tougher in compression than out-of-plane honeycomb structures, but unlike honeycombs, 8-cell tesseracts are 3D structures with cubic symmetry. Architecture has a profound effect on the relative consistency of properties with cubically symmetric structures displaying the greatest levels of consistency in terms of both strength and stiffness reduction as a function of pore space. The results presented in this paper showcase the potential of this new class of mechanical metamaterial based on 3D projected 4-polytopes.

Keywords: Machine learning, Genetic Algorithm, Mechanical Metamaterial, Cellular Solids, 3D printing, Parametric Optimisation

1. Introduction

Mechanical metamaterials are artificial structures designed to enhance a chosen material property or behaviour. This is achieved through the manipulation of internal substructures to enable a calculated mechanical response that goes beyond the ordinary response of the base material. Common examples include metamaterials with auxetic behaviour [1, 2, 3], with an enhanced compressive response [4, 5], with high energy absorption capacity [6, 7] and with high stiffness and strength properties [8, 9, 10, 11]. Relatively recent advancements in additive manufacturing technologies have accelerated our capacity to manufacture and test mechanical metamaterials, which were previously too expensive, complex or cumbersome to produce. This in turn has created a new avenue for the exploration of complex metamaterial substructures using AI and optimisation approaches [12, 13, 14, 15]. Meta-structure optimisation methods have previously employed finite element analysis (FEA) as a basis for structure-property enhancements [16, 17]. These include non-linear programming [18], gradient-descent [19, 20, 21], Bayesian optimisation [22, 23], deep learning [24, 25] and various evolutionary algorithms [26, 27, 28, 29, 30] as a basis for the optimisation frameworks. These optimisation frameworks rely on topology [31, 3, 17, 25] and parametric design approaches [22, 26, 32, 33, 34, 5] to alter the arrangement of metamaterial lattices [23, 4], chiral structures [34, 32] and thin-walled cellular solids

*Corresponding author
Email addresses: g.cerniauskas@ed.ac.uk (Gabrielis Cerniauskas), parvez.alam@ed.ac.uk (Parvez Alam)

[6, 7, 8]. While there are a few reports detailing the design of mechanical metamaterials based on fractal substructures [35, 36, 37, 34], 3D projections of 4th dimensional geometries (4-polytopes, or, polychorons) have not as yet been considered as baselines for the design of novel, structural mechanical metamaterials. Yet, a 3D projection of a 4th dimensional geometry (4-polytope) is inherently fractal in its construction, with increased fractalisation arising as a function of any additional n^{th} dimension integer of an n-polytope. 3D projections of 4-polytopes are essentially geometrical structures that are 4D projections of 3D polyhedra. Their self-repeating, fractal, substructures are hierarchical in nature and potentialise mechanical suitability in structural applications, where the coupling of lightweightness and load bearing is desired [34, 38, 35]. Due to their geometrical symmetry and self-repeating features when projected as 3D structures, 4-polytopes have been of interest in aesthetic design and can be seen in some patterned materials, ornaments and creative sculptures [39, 40, 41]. While there also are numerous reports on the more technical utility of 4-polytopes, for example as space discretising finite elements [42, 43, 44, 45], and even one as an additively manufactured high-porosity potential bone replacement material [46], Choi and Lee [47] provide the only report detailing relationships between the porosity and stiffness, and the porosity and strength of hypercubes, or, tesseracts. In their work, they discuss the strength and stiffness of strut-based hypercubes in terms of $\left(\frac{E*}{E_s}\right) = C\left(\frac{\rho*}{\rho_s}\right)^a$ and $\left(\frac{\sigma*}{\sigma_s}\right) = D\left(\frac{\rho*}{\rho_s}\right)^b$, respectively, where E, σ and ρ are the Young's modulus, the strength in compression and the density, respectively. The symbols $*$ and $_s$ represent the hypercube including pore space, and the bulk constituent solid material, respectively. C, D, a and b are constants and it should be noted that in their paper, both a and b are values > 1, indicating that the variation in mechanical properties with pore space is nonlinear. There is an obvious gap in knowledge concerning the development of 4-polytope projected mechanical metamaterials, which this paper aims to address. The work presented herein considers the suitability of 4-polytope projections as basal structures for the development of novel mechanical metamaterials. The contributions from this work are two-fold as it introduces a new class of metamaterial and proposes an optimisation and metamaterial design framework based on a single-objective genetic algorithm. Firstly, to the best of our knowledge, this paper pioneers the adoption of 4D polytope theory in mechanical metamaterial design. Secondly, we introduce a design and simulation framework featuring a genetic-algorithm-based parametric optimisation methodology that can be used to enhance a chosen mechanical property. In this paper, our objective function focusses on maximising specific stiffness. Our concurrent interest is to determine how a focus on maximising specific stiffness via stored energy principles, might affect other mechanical properties of optimised 3D projected 4-polytopes.

2. Methods

2.1. Design of 4-polytope projected structures

Four regular convex 4-polytopes were considered in this paper, as baseline geometries for the design of advanced mechanical metamaterial architectures. These are shown in Figure 1 as 5-cell (pentatope), 8-cell (tesseract), 16-cell (orthoplex) and 24-cell (octaplex) structures. As can be seen in this figure, Schlegel diagrams were used to project the 4D geometry as a perspective in 3D space. The method essentially reduces a 4-polytope from 4D to 3D by taking a single projection of the geometry and displaying it as a wire-frame in 3D space (3D projected 4-polytope, or, 4-polytope projection). Each one of the four wire-frame representations of the 4-polytopes shown in Figure 1 was used to develop a single metamaterial unit cell by taking the wire-frame edges and vertices to define the geometry of the thin-walled metamaterials. As the wire-frame rendering of the 4-polytopes only provides a geometrical silhouette, the thin-wall features were rendered to match the boundaries of the 4-polytope cell projection as closely as possible. This ensured that the generated thin-walled structures had multiple planes of geometrical symmetry (cubic symmetry of a single cell). The wire-frame structures and their equivalent thin-walled unit cells are shown in Figure 1. The unit cells designed using this approach provide a lot of design flexibility in terms of the structural parameters. As the wire-frame representation only illustrates the location of the 4-polytope vertices and edges in the Euclidean space, adding thickness to a wire-frame structure allows for the generation of multiple thin-walled metamaterial geometries that originate from the same 4-polytope projection. Additionally, the depth of the perspective can be changed which keeps the same symmetry of the unit cell but results in shrinking or enlarging of the geometrical primitive in the middle of each cell (e.g. the inner cube in the 8-cell). Therefore, by changing the parameters such unit cell wall thickness and the internal geometry angles, the core geometrical shape of the 4-polytope projection is maintained and numerous metamaterial unit cell geometries are generated. As an example, the 5-cell structure was defined using 10 parameters that could be varied to alter the geometrical features in terms of size and shape.

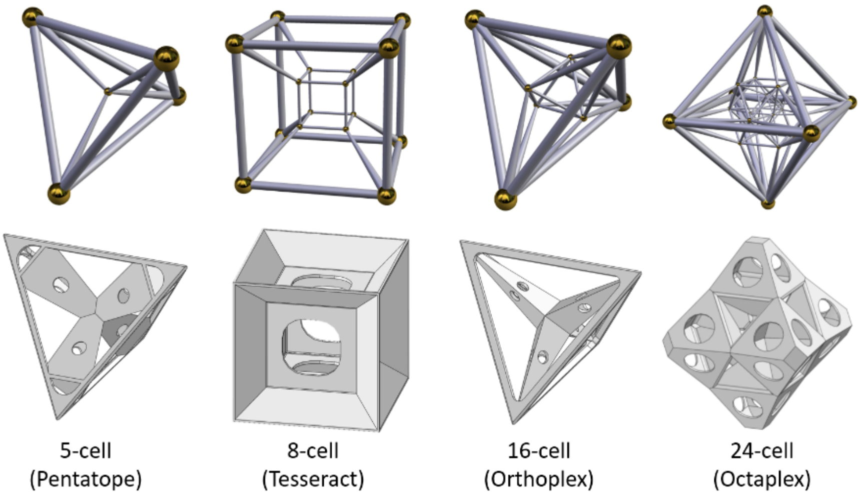

Figure 1: Wire-frame Schlegel diagrams (perspective projection) of regular convex 4-polytopes (top) and the 4-polytope projections designed using the wireframe diagrams (bottom).

Drain holes were introduced to ensure compatibility with the low force stereolithography (LFS) additive manufacturing process to allow for a free flow of resin around and inside the thin-walled structures during the printing process. Design parameters for each of the unit cells are shown in Figure 2 and these are described in greater detail in Table 1. By using this parametric approach to design, the generation of unit cell structures could be automated, as could any geometrical adjustments necessary in response to loading. The exterior dimensions of a unit cell were not varied as unit cells had to form arrays and these were thus defined by fitting a unit cell into a bounding box cube with an edge length of 10mm. This ensured that the unit cells could be stacked in linear arrays to form larger structures comprised of identical repeating unit cells.

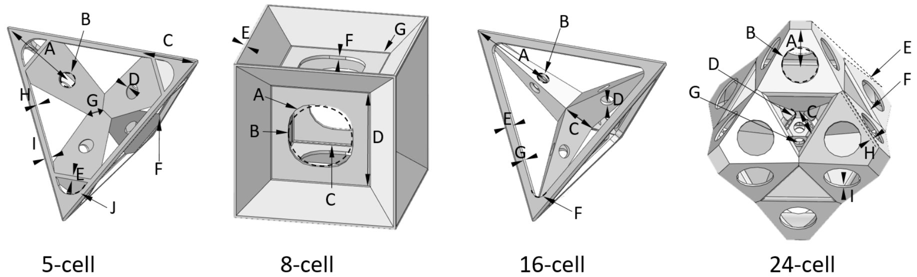

Figure 2: Parametric design approach to 4-polytope projected metamaterial design. Adjustable parameters are marked in letters for each structure.

2.2. Unit cell simulation and parametric optimisation

Finite element analyses were conducted using Abaqus/Implicit (Dassault Systémes) to determine the properties of each of the 3D projected 4-polytopes subjected to compressive elasto-plastic loading. The compressive mechanical properties of a Formlabs Clear Resin were input into the model as follows: Young's modulus = 2.03 GPa, Poisson's ratio = 0.38 and density = 1.164g/cm^3. When the model reaches its compressive yield strength, σ_y, of 72.28 MPa, it undergoes strain softening behaviour over the plastic region of the stress-strain curve, which was approximated as $\sigma_y = 44.99 \times \epsilon_y^{-0.142}$, where ϵ_y is yield strain. The Newton-Raphson method was used with an implicit solver as it allowed for variable size time increments that were well suited to the simulation problem, providing an accurate solution whilst minimising computational time as compared to an explicit solver. Boundary conditions were applied to

Table 1: Parametric design variables for 5, 8, 16 and 24-cell designs as illustrated in Figure 2.

5-cell		8-cell		16-cell		24-cell	
A	Drain hole distance	A	Drain hole round radius	A	Drain hole distance	A	Drain hole distance
B	Drain hole radius	B	Drain hole radius	B	Drain hole radius	B	Drain hole radius
C	Corner distance	C	Inner edge round radius	C	Inner triangle size	C	Inner triangle size
D	Inner wall thickness	D	Inner cube size	D	Inner wall thickness	D	Inner triangle round
E	Corner wall thickness	E	Outer wall thickness	E	Outer shell width	E	Projection angle
F	Outer corner round	F	Inner cube wall thickness	F	Outer shell round	F	Outer shell round
G	Inner triangle size	G	Outer edge round radius	G	Outer shell width	G	Inner wall thickness
H	Outer shell thickness					H	Middle wall thickness
I	Outer shell width					I	Outer wall thickness
J	Outer shell round						

one quarter of each of the 3D projected 4-polytope unit cells, thus taking advantage of the geometrical symmetries to lessen the computational expense. The modelled sections were considered central cells within blocks of neighbouring cells and as such, the outer surfaces of each unit cell were ascribed symmetry boundary conditions about the planes located at the outermost faces of the unit cells, i.e. the interfaces of adjacent unit cells, Figure 3. As can be observed in this figure, symmetry boundaries were assigned about the inner X (black dashed line) and Z (yellow dashed line) planes. The bottom surface of each unit cell was assigned an encastre boundary condition ($U1 = U2 = U3 = UR1 = UR2 = UR3 = 0$), where U is translation in axes 1, 2 and 3 and UR is rotation about axes 1, 2 and 3. A displacement condition was assigned to the upper surface of each unit cell to a maximum unit cell compressive strain of 0.08. A tetrahedral mesh element (C3D10) was chosen to discretise the structures. A free meshing technique was used as it was found to be the most flexible for meshing when compared against structured and swept meshing approaches. The mesh density was chosen based on a mesh convergence study carried out for each of the 3D projected 4-polytope models, and a mesh growth rate of 1.05 was consequently used to obtain evenly sized elements. Remeshing was introduced by seeding the edges of the geometry. A minimum constraint of three elements across the thinnest feature was implemented and the number of elements increased as the size of any particular geometrical feature increased. This resulted in a mesh density that was fine enough to capture the through-thickness response of the thin-walled features, whilst keeping the number of elements in each model to a minimum.

With the unit cell simulations set up, the optimisation framework was built to automate exploration of the design space. Manufacturing constraints were incorporated to avoid exploring structures that could not be produced using the low force stereolithography prototyping method. Two constraints were implemented, namely: (1) minimum thin wall thickness, which was constrained by the force required to peel the print off the resin tank between each layer printing and (2) minimum drain hole diameter, which was limited by the resin viscosity to allow sufficient flow rate and hence draining of hollow chambers within the thin-walled structures. Therefore to reduce the overall computational time, structures with features that were too small to produce, or, which resulted in suction cups (concave features restricting resin flow around the printed part causing failed prints) were excluded from the design space exploration. The manufacturing approach is further discussed in Section 2.3.

The 5, 8, 16 and 24-cell 4-polytope projections were optimised for specific stiffness, $\frac{E}{\rho}$, where E is the elastic modulus of the structure in compression, and ρ is the apparent density of the structure. This was achieved by combining the finite element simulations with an evolutionary algorithm based optimisation approach. The core of the framework is a single metamaterial unit cell simulated in compression using the design parameters, described in Figure 2 and Table 1, as inputs for the FE analysis, and strain energy, U, and mass of the total structure, m, measures as outputs from the simulation. When run, the optimisation algorithm adjusts the input design parameters and iterates the simulation process to determine a final structure exhibiting the highest specific stiffness, which in its simplest form is expressed in Equation 1, where V is the total volume of the structure and σ is the 1st Piola-Kirchhoff stress and U_e is the elastic strain energy. The evolutionary algorithm employed to avoid brute force explorations of the design space was a single-objective genetic algorithm (GA). The parametric design variables for each consecutive generation of unit cell designs were based on the stored solutions of simulation results from preceding runs. The purpose of the GA was to find a unit cell arrangement demonstrating the highest specific stiffness properties in compression. The

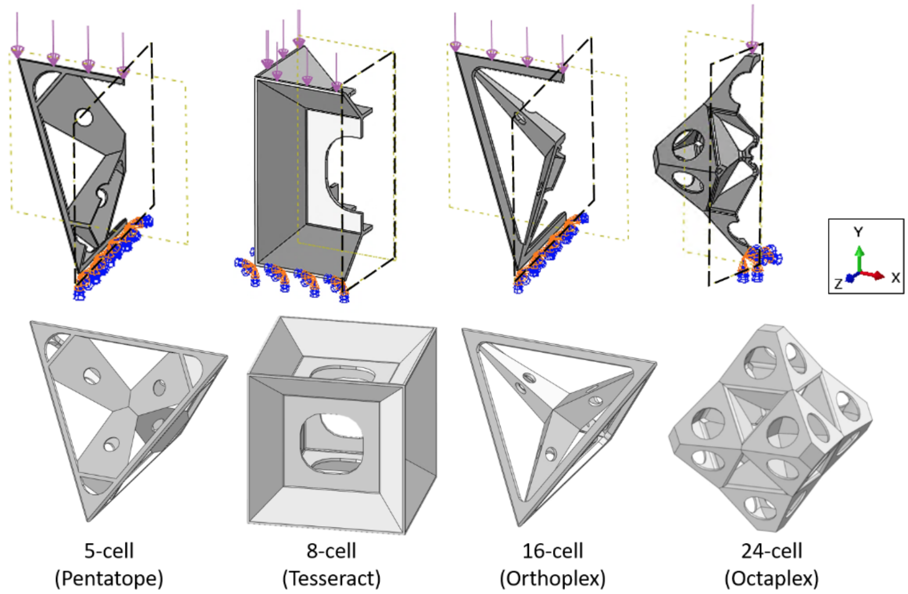

Figure 3: Boundary conditions of FEA models for 5, 8, 16, 24-cell metamaterial cells (top) and equivalent 4-polytope based unit cells (bottom). The outer surfaces of a unit cell were prescribed symmetry boundary conditions about the X and Z planes located at the interface between the two adjacent cells. A quarter of each unit cell was modelled by using the internal symmetry planes which are marked in yellow (symmetry about a plane Z) and black (symmetry about a plane X) dashed lines with encastre boundary condition at a bottom and displacement resulting in a unit cell compressive strain of 0.08 at the top of the cell.

objective function was formulated using U_e as an output to satisfy the objective function and is computed according to Equation 2. Here, V_e is the volume of an element, n is the number of elements in a model, $\boldsymbol{\sigma_{ij}}$ is the stress tensor of an element, and $\boldsymbol{\epsilon_{ij}}$ is the elastic strain tensor of an element. The process is completed when the objective function is realised, which here, is defined by the strain energy and mass measure outputs from the FE simulations as these parameters are to determine the final value of $\frac{E}{\rho}$. The process is iterated multiple times to assess the wide range of possible designs and to source the structure exhibiting the maximum $\frac{E}{\rho}$ value. The algorithm then makes use of the output from finite element analyses to evaluate the existing population of the metamaterial structures, selecting the best performing designs and subsequently using crossover and mutation to generate a new population. These steps were executed multiple times until a stop-criterion was met and the near optimum design was found. A schematic flow diagram of the algorithm is shown in Figure 4.

$$\frac{E}{\rho} = \left(\frac{\sigma^2 V}{2U_e}\right)\left(\frac{m}{V}\right)^{-1} \tag{1}$$

$$U_e = \sum_{e=1}^{n} V_e \cdot \int_0^{\epsilon_{ij}} \sigma_{ij} d\epsilon_{ij} \tag{2}$$

The GA set up used a population size of 28, the choice of which was based on the number of genes, simulation complexity, and available parallel processing units. The absolute number of generations was set to 50, however, the optimisation had a built in stop-criterion which was activated when the results showed no improvement over the next 20% of the total generation number from the best solution. This stop-criterion was built in to reduce the computational costs of the optimisation and therefore reduce the design time. Each of the four structures presented herein reached the stop-criterion in under 756 design iterations. Crossover probability, mutation probability, and crossover and mutation distribution indices were set to 0.9, 1/q, 10 and 20, respectively, where q is the number of parametric design variables. GA parameter tuning was not carried out for this design problem as it was deemed beyond the scope of this paper and

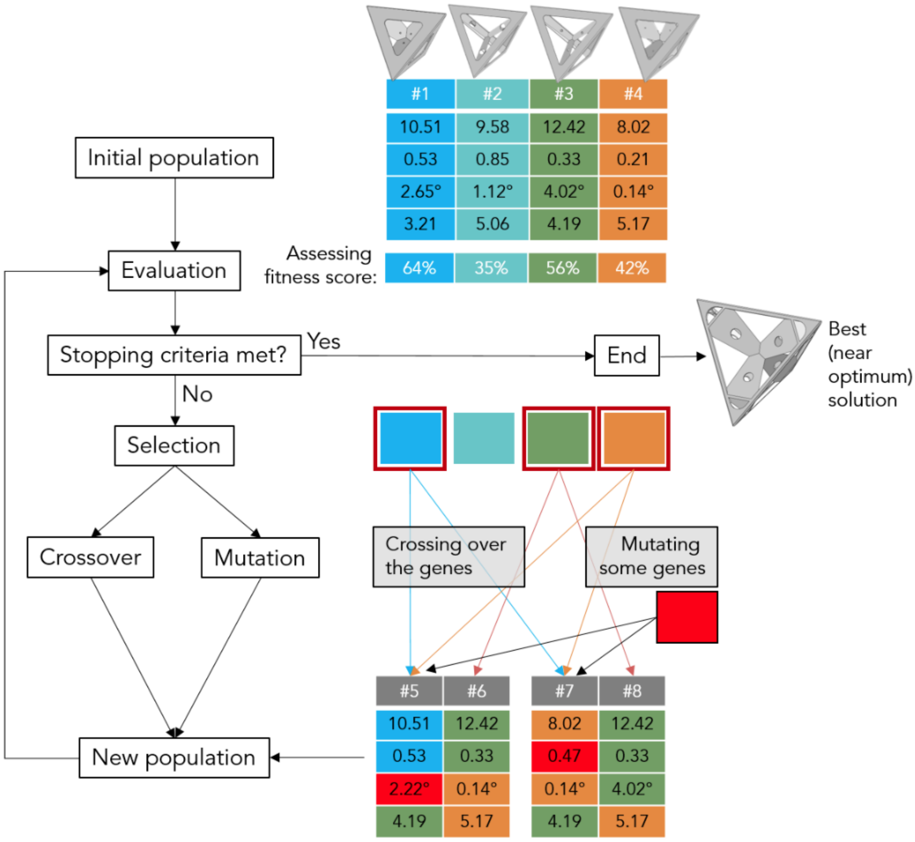

Figure 4: Schematic representation of genetic algorithm used in the optimisation framework.

the values were chosen to fit a universal design problem based on previously available knowledge [13]. The algorithm parameters chosen for this optimisation problem are summarised in Table 2.

Table 2: Summary of the parameters used in genetic algorithm set-up.

GA parameters:	
Population size	28
Abs. no. of generations	50
Crossover probability	0.9
Mutation probability*	1/q
Crossover distribution index	10
Mutation distribution index	20
Stopping criteria	no improvement in last 20% of gen.

*q is the number of design variables

2.3. *Manufacture*

Experimental samples were manufactured using a photoreactive thermoseting resin (Clear V4) developed for low force stereolithography (LFS) 3D printing by Formlabs. The samples were printed using a Form 3 printer and the unit cells discussed in Section 2.1 were stacked to create an array comprising $5 \times 5 \times 5$ unit cells. Each specimen thence consisted of 125 unit cells and had the external dimensions of $50 \times 50 \times 50$ mm. The Form 3 printer layer height was set to 25μm. After the 3D printing process, the samples were washed in isopropyl alcohol using a Form Wash to ensure that uncured resin was removed from the samples. Samples were then post-cured in a Form Cure at 60°C in a UV light chamber for 30 minutes to increase the stability and strength of the parts, as suggested by the resin manufacturer. The samples were found to have high dimensional accuracy when compared against the CAD models, with a deviation of less than 0.3%. The weight of the structures was consistent between the same geometry samples, however, these can vary between the different unit cell design samples due to areas of uncured or partially-cured resin not being accessible for washing as a result of the complex internal unit cell geometries. Accumulated resin that cannot be washed can therefore be cured during the post-curing process of the specimens, which can consequently increase the total weight of the structures and which may also alter the shape of the solid features. To circumvent this problem, the washing procedure was adjusted for each specimen type so as to minimise the resin residue inside the specimens. The weight variation, Δw, of the final cured specimens compared to the expected weight computed from the CAD model volumes was calculated as $\Delta w = \left(\frac{w_{sample}}{w_{CAD}} - 1\right)$, where w_{sample} is the measured weight of the cured sample and w_{CAD} is the calculated weight of the sample based on the product of the computed CAD model volume and the cured density of Clear V4 resin. Δw was thus found to be 0.075, 0.076, 0.13 and 0.12 for the 5-cell, 8-cell, 16-cell and 24-cell samples, respectively.

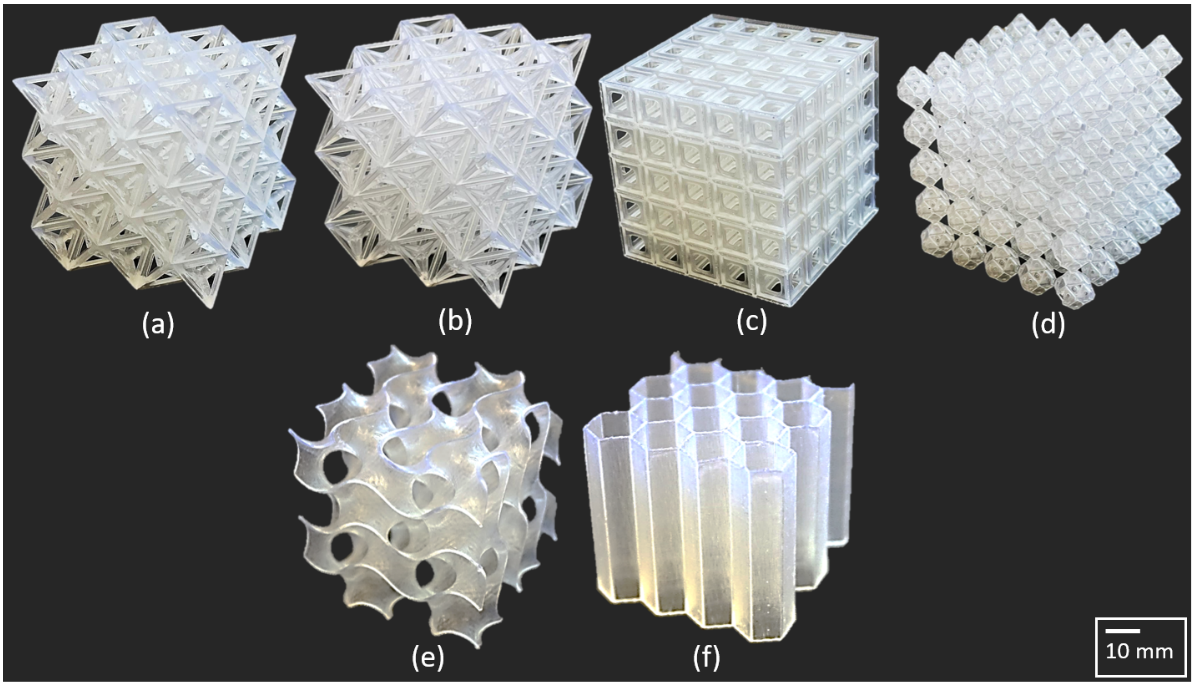

Figure 5: Representative compressive test specimens with a $5 \times 5 \times 5$ 3D projected 4-polytope unit cell array: (a) 5-cell, (b) 8-cell, (c) 16-cell and (d) 24-cell, and additional structures used as 'comparative experimental controls' also in a $5 \times 5 \times 5$ array: (e) gyroid and (f) hexagonal honeycomb (tested in the out-of-plane direction).

Sets of $5 \times 5 \times 5$ honeycomb and gyroid samples were additionally manufactured as a means of comparing the mechanical behaviour and properties of 3D projected 4-polytopes against more commonly researched cellular solid structures. The same resin and manufacturing technique was used as described for the 4-polytope projections, and representatives of each are shown in Figure 5. 3D printed honeycomb samples had a cell size of 8.5mm, wall thickness of 0.5mm, sample thickness of 30mm, volume fraction of 12.24% and an apparent density of 144 kg/m^3. The gyroid samples were designed using a sinusoidal curve with an amplitude of 5.5mm and period of 20mm. The wall thickness was 0.5mm, which resulted in a sample volume fraction of 7.68% and an apparent density of 89 kg/m^3.

2.4. Mechanical testing

An Instron 3369 mechanical test machine with a load cell of 50kN was used to test the samples in compression between two horizontal compression platens. Strain measurements were taken using a 2D digital image correlation technique (Imetrum DIC system with 1400×1000 resolution at 17.8fps). The strain measurements were taken across both vertical and horizontal outermost faces of the nine surface unit cells in the middle of the 5×5 metamaterial cell array, and were averaged to obtain strains in the axial and the transverse directions. Although the measurements were taken on the outermost surfaces of the specimen, this approach ensured that the output strain values were less affected by free surface effects at the boundaries of the samples. Five specimens, manufactured in the same manner, were tested for each of the 4-polytope projected metamaterials, as well as for each of the gyroid and honeycomb structures (tested out-of-plane). All samples were tested at a ramp rate of 10mm/min, a rate at which cured neat resin exhibits Hookean behaviour under deformation.

3. Results and Discussion

3.1. Simulation results

As discussed in Section 2.2, the simulation-based optimisation framework generated a set of metamaterial structures for each 3D projected 4-polytope geometry. The performance of each was assessed and ranked according to the objective function, which evaluated the specific stiffness of each structure. Figure 6 summarises the performance of four sets of 4-polytope projected geometries and illustrates the incremental progression of each at different stages of the optimisation process. The colours in the bar chart represent the specific stiffness of (i) an unoptimised structure (0%), (ii) 33% of full optimisation, (iii) 67% of full optimisation and (iv) a fully optimised (100%) structure. As the algorithm explores the design space, the specific stiffness of the structures can be seen to increase for each of the 3D projected 4-polytopes. The performance enhancement between the unoptimised and fully optimised structures are 64.74%, 38.40%, 137.12% and 78.18% for the 5-cell, 8-cell, 16-cell and 24-cell metamaterial structures. The metamaterial structure with the highest specific stiffness at 100% optimisation is found to be the 8-cell, followed by the 5-cell, 16-cell and 24-cell, in that order. Since the 8-cell also has the lowest level of post-optimisation improvement when compared to the other structures, it shows that the 3D projected tesseract is already a highly advanced 3D projection with excellent properties of stiffness against density.

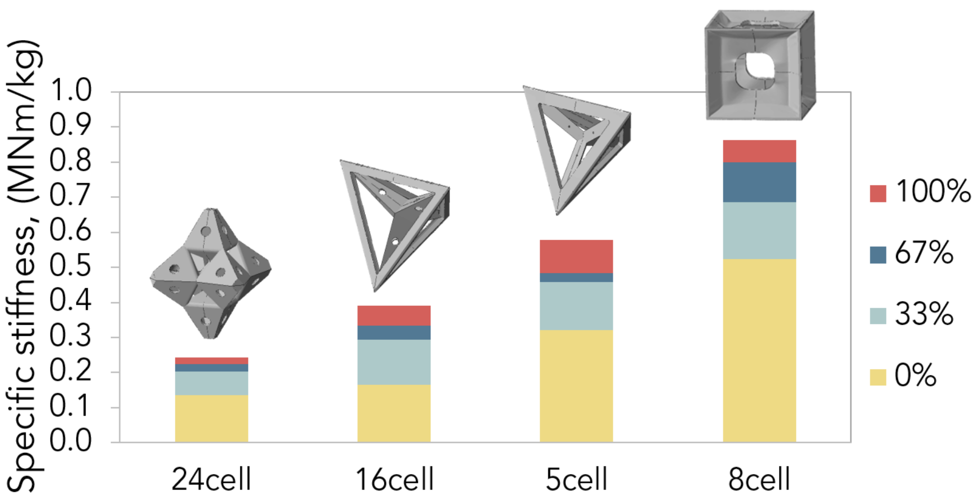

Figure 6: Increases in specific stiffness with incremental optimisation progression from the unoptimised (0%) to the fully-optimised (100%) iteration for 24, 16, 5 and 8-cell metamaterial structures, in that order.

To better understand these results, the strain energy density was assessed in relation to the overall energy storage capacity of each 3D projected 4-polytope structure over the optimisation process. Figure 7 shows the 5-cell, 8-cell,

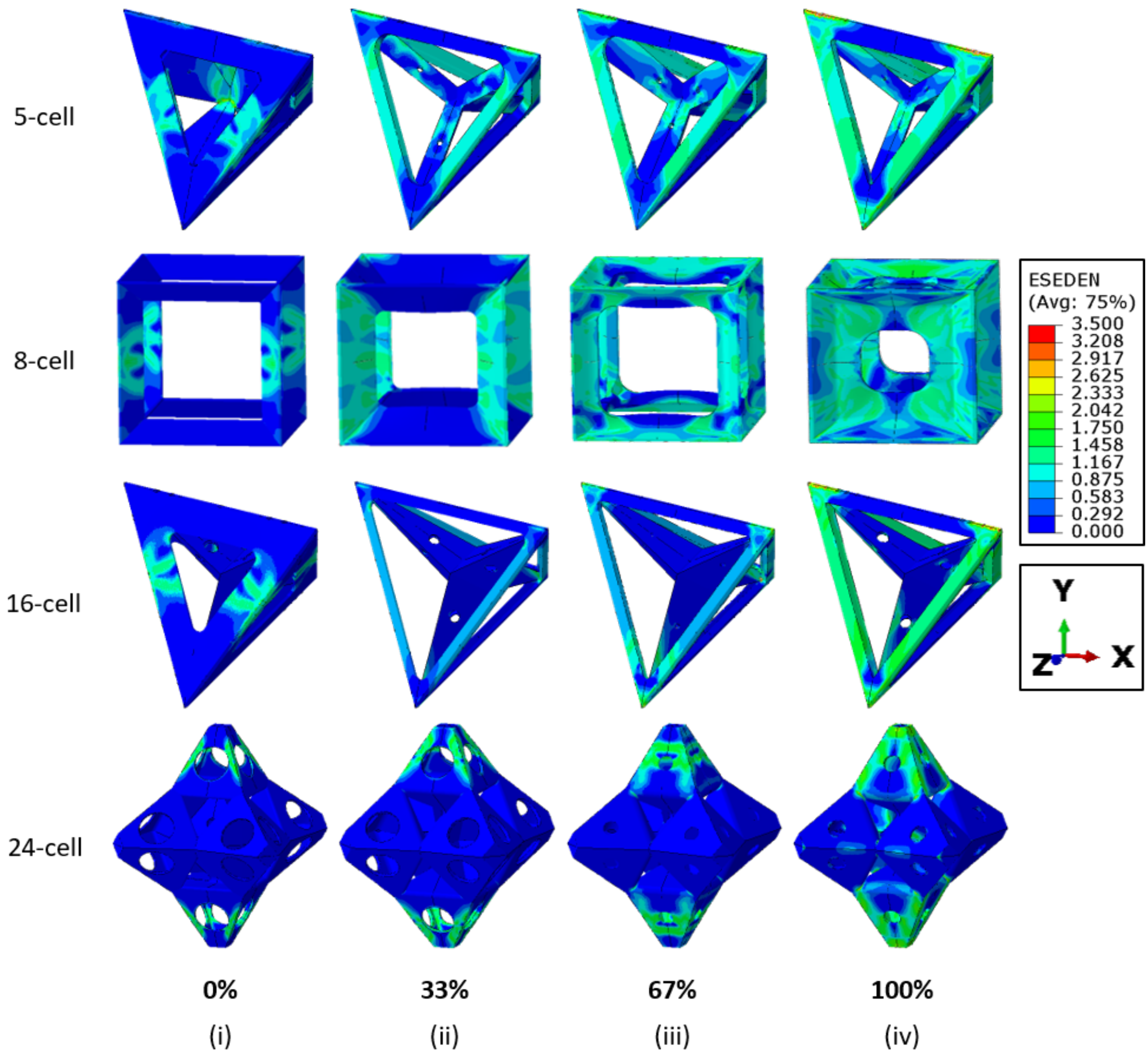

Figure 7: Comparison of optimised 4-polytope projected models with labels (i) to (iv) representing optimisation level: 0% (unoptimised), 33%, 67% and 100% (fully-optimised) structures, respectively. The colour map shows the elastic strain energy density (ESEDEN) distribution in J/cm^3 at the compression strain of 0.08 in each structure.

16-cell and 24-cell structures at (i) 0% (ii) 33% (iii) 67% and (iv) 100% of the total optimisation. The colour map illustrates the distribution of elastic strain energy density within each structure and indicates the geometrical regions of each structure that contribute the most towards load-bearing under axial compression. Strain energy can be seen to distribute through more of the solid state continuum from the unoptimised structures through to the fully optimised structures. As such, the total stored elastic strain energy increases for each structure with respect to the increasing level of geometrical optimisation. As the ability to store elastic strain energy correlates directly with metamaterial stiffness, the fully optimised structures consequently exhibit the highest stiffness values. When factored against their final apparent densities, we find that the fully-optimised structures in each set also have the highest specific stiffness values within each set as shown previously in Figure 6. The fully-optimised structures that distribute strain energy more effectively through the solid state continuum of each structure (5-cell and 8-cell) also absorb higher levels of elastic strain energy and this contributes to their higher compressive modulus and thus higher specific stiffness values. Structures with more localised strain energy (16-cell and 24-cell) have comparatively lower specific stiffness values. This is related to the effectiveness in the distribution of elastic strain energy through a greater volume of the body of the material, which is therefore a key design consideration as it contributes towards the overall stiffness of the structure. Structures comprising lower levels of internal geometrical complexity (5-cell and 8-cell) are noticeably more resistant to compressive loading than more complex structures (16-cell and 24-cell). This is primarily because 3D projected 4-polytope metamaterials with higher levels of geometrical complexity have more slender edges and sharper corner features. This combination of geometrical features results in the localisation of higher strain energies at lower loads.

3.2. Experimental testing results

Figure 8 plots the experimentally measured specific stiffness values against experimental specific yield strength values for each of the 3D projected 4-polytopes. The arithmetic mean of each specific property is shown based on five specimens tested for each structure (n = 5), and the vertical and horizontal bars represent the total range of measured experimental values for each measured property. To enable comparison against more common structures, the chart includes the data points for the 3-dimensional cubically symmetrical gyroids, and the hexagonal honeycomb structures (tested out-of-plane), which were manufactured in the same way as the 4-polytope projected metamaterials (cf. Section 2.3). In this figure, 3D projected 4-polytopes follow the same trend as has been predicted by the simulations. The 8-cell metamaterials exhibit the highest specific stiffness with an average value of 0.68 MNm/kg, followed by the 5, 16 and 24-cell metamaterials, which have average values of 0.43, 0.28 and 0.19 MNm/kg, respectively. The experimental results furthermore indicate that the specific yield strength values follow a similar trend with the 8-cell metamaterials having the highest value of 22.8 kNm/kg, followed by the 5-cell, 16-cell and 24-cell metamaterials. Metamaterial designs with (a) less complex internal structures and (b) geometric features more closely in-line with the direction of loading, perform noticeably better in terms of specific stiffness and specific yield strength. Such a trend aligns well with the strain energy density results summarised in Figure 7, which showed that the structures with a less distributed strain energy density have a lower overall capacity to store strain energy and hence exhibit a lower overall stiffness.

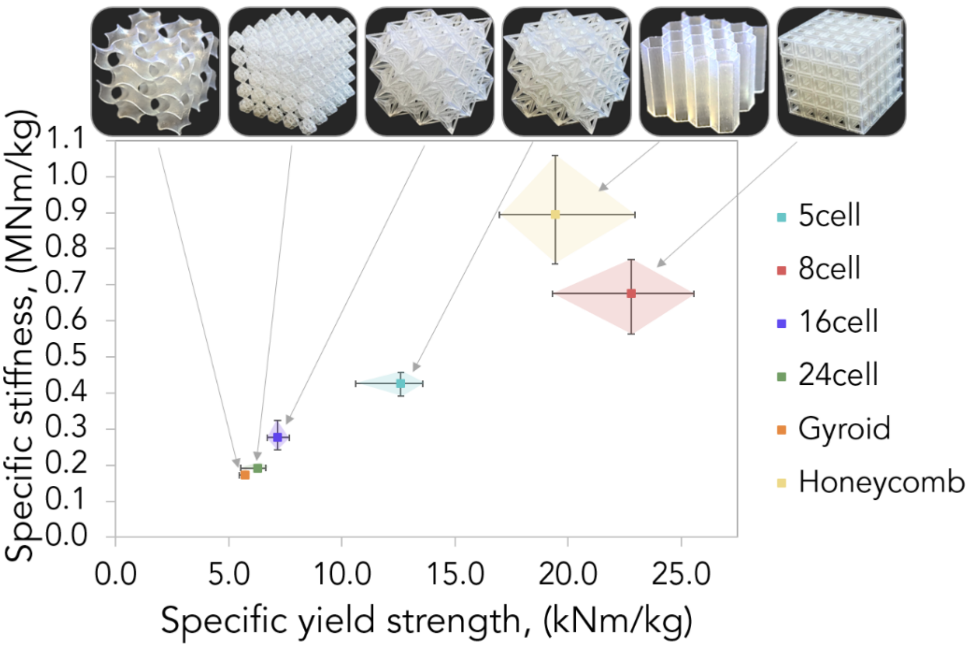

Figure 8: Comparison of experimental results of 4-polytope projected metamaterials to honeycomb and gyroid structures (n = 5).

Figure 8 also demonstrates that each of the 3D projected 4-polytope metamaterials outperform a cubically symmetric 3D gyroid in terms of both specific stiffness and specific yield strength. All structures exhibit a lower specific stiffness than a hexagonal honeycomb tested in the out-of-plane direction, however, it should also be noted that there is overlap between the 8-cell and honeycomb error bars and as such the best of the experimental 8-cell metamaterials are as high in specific stiffness as the least of the honeycomb structures tested out-of-plane. In addition, the 8-cell tesseract outperforms the hexagonal honeycomb by 17.3% in terms of its specific yield strength. This is due to that the 8-cell metamaterial has thin-wall features oriented in the axis of loading, in a similar manner to those of the hexagonal honeycomb when loaded in an out-of-plane direction. An arrangement of this kind benefits both the overall stiffness and strength of a structure and additionally, the optimised geometry of the 8-cell metamaterial minimises any internal stress concentrations. The combination of the two aforementioned factors is plausibly the reason for why the 8-cell metamaterial has such a high specific yield strength. One significant difference between the 3D projected 4-polytope metamaterials and the out-of-plane honeycomb, is that the 4-polytope projected metamaterials have the same mechanical properties in all three orthogonal axes (i.e. they are cubically symmetric). This is highly dissimilar to the honeycomb structures, which are essentially 2D hexagonal packings extruded orthogonally in a 3rd axis. While they have a very high specific stiffness in the out-of-plane direction, they are also very weak and of low stiffness in their in-plane axes, deforming significantly when loaded in-plane [35].

Tables 3 and 4, provide experimental and simulation results for specific stiffnesses and specific yield strengths, respectively. Statistical details are included for the experimental phases of the work (experimental range, standard deviation and the coefficient of variance (CoV)), and a comparison is also made between the simulation results for each sample set as a percentage difference and a Z-score (Z), where in the case of specific stiffness, $Z = \frac{\frac{E}{\rho} - \frac{\bar{E}}{\rho}}{S}$ and in the case of specific yield strength, $Z = \frac{\frac{\sigma_y}{\rho} - \frac{\bar{\sigma_y}}{\rho}}{S}$, and S is the standard deviation of the sample set. From these tables, we note that the simulations are overall between 18.9% and 28.2% different from the arithmetic mean of the sample sets when comparing for specific stiffness, and between 9.8% and 22.9% different from the arithmetic mean of the sample sets when comparing for specific yield strength. The Z-scores range between 2.88 and 8.33, and 1.21 and 5.57 when comparing between simulation and experiment for specific stiffness and specific yield strength, respectively. The simulated specific yield strength results are also the most accurate for the 8-cell metamaterial with the percentage difference from the experimental results being 9.82%, while the values for the 5-cell, 16-cell and 24-cell were found to be 19.95%, 22.94% and 20.51% respectively. Following the same trend, the 8-cell based structure has the lowest Z-score value of 1.21 while the 16-cell has the highest value of 5.57. The 8-cell structures have the lowest Z-score in each case (2.88 and 1.21) indicating that the 8-cell manufactured samples are the closest in properties to the properties predicted through simulation. Figure 9 shows how the simulated stress-strain curves for each of the 4-polytope projections tend to lie closer to the upper bound of the experimental ranges in each sample set. While the stress-strain curves of the 8-cell, 16-cell and 24-cell simulations are reasonably close to the experimental curves, the 5-cell simulations are less correlated with the experimental test results. Reasons for why the experimental stress-strain curves are generally slightly lower than the simulation curves most likely originates from limitations related to specimen manufacture. As discussed in section 2.3, the specimen weight was found to be higher than the model mass due to surplus resin that accumulated within the 3D printed structures. Inconsistencies in resin deposition are a plausible cause for unpredicated stress distributions leading to the development of stress concentrations. In addition to this, since in the post-curing process, samples are exposed to heat and UV light to increase the cross-linking of the polymer, the post-curing rate of each 4-polytope projection is unique, as curing is affected by the distinctive geometry of a structure, and its surface area to volume ratio. As such, there are variable levels of curing not only within individual samples, but also between the different sample sets. Variability between the samples is obvious from the experimental results in Figure 9 and since the simulation results represent fully cured, and ideally cured structures, the simulation predictions will naturally tend towards a more mechanically ideal upper bound from the experimentally measured samples.

The specific properties discussed thus far have been achieved by means of maximising the elastic energy stored in each of the 4-polytope projections. Ascertaining how a focus on strain energy optimisation might also impact other mechanical properties is a worthwhile exercise, as it allows for the further comparison of 4-polytope projected metamaterials over a wider range of mechanical properties. Representative compressive stress-strain curves from each of the experimental tests are provided in Figure 10 (a) and the following properties are compared in Table 5: Young's modulus (in compression), yield strength, compressive strength, modulus of resilience, and the modulus of

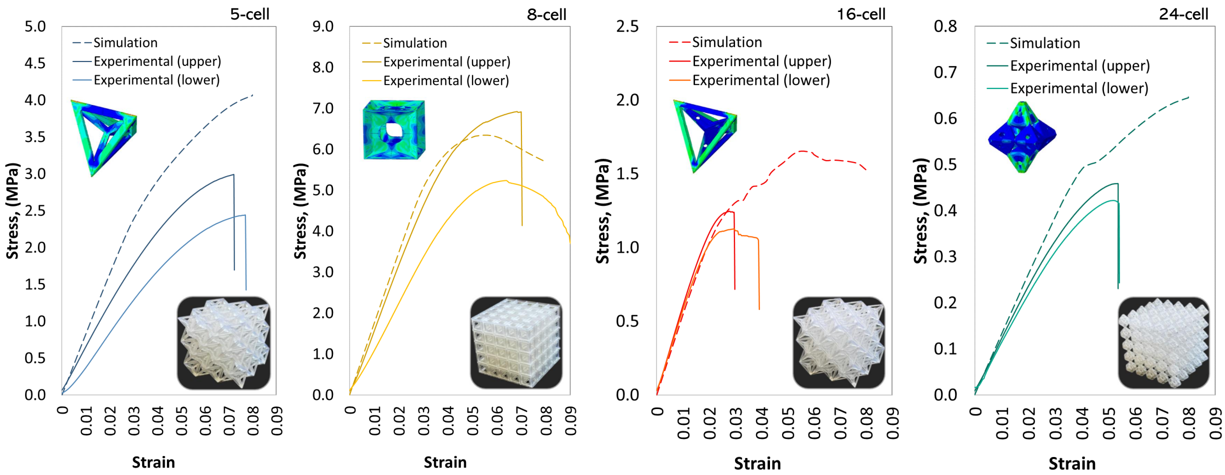

Figure 9: Upper and lower experimental bound stress-strain curves, and simulation stress-strain curves for 5-cell, 8-cell, 16-cell and 24-cell 4-polytope projections.

Table 3: Mean specific stiffness values $\left(\frac{\bar{E}}{\rho}\right)$ results for experimental samples: 5, 8, 16 and 24-cell metamaterials, as well as gyroid and honeycomb structures and specific stiffness values $\left(\frac{E}{\rho}\right)$ for simulated models: 5, 8, 16 and 24-cell metamaterials.

Experimental	5-cell	8-cell	16-cell	24-cell	Gyroid	Hex honeycomb
Mean specific stiffness $\left(\frac{\bar{E}}{\rho}\right)$ (MNm/kg)	0.43	0.68	0.28	0.19	0.17	0.89
Upper value	0.46	0.77	0.33	0.20	0.17	1.06
Lower value	0.39	0.56	0.24	0.18	0.17	0.76
Median	0.42	0.68	0.27	0.19	0.17	0.91
Standard deviation	0.022	0.066	0.028	0.006	0.001	0.100
CoV	5.09%	9.80%	10.01%	3.37%	0.85%	11.17%

Simulation						
Specific stiffness $\left(\frac{E}{\rho}\right)$ (MNm/kg)	0.53	0.87	0.39	0.24	N/A	N/A
Percentage diff. (sim. vs exp.)	18.9%	21.8%	28.2%	20.8%	N/A	N/A
Z-score	4.55	2.88	3.93	8.33	N/A	N/A

toughness. The standard deviation (SD) and the coefficient of variation (CoV) are also provided for each property in each sample set. The experimental 8-cell metamaterial samples exhibit the highest mean Young's modulus out of all of the sample sets at 145.01 MPa. This is 12.6% higher when compared against the mean Young's modulus of the hexagonal honeycomb, which was 128.75 MPa out-of-plane. The 5-cell and 16-cell based metamaterials outperform the gyroid samples exhibiting mean Young's modulus values of 70.53, 43.52 and 15.30 MPa, respectively. The structure with the lowest stiffness out of the 4-polytope projections is the 24-cell, which has a mean Young's modulus of 11.73 MPa. The CoV ranges between 0.85% and 11.17% for all sample sets, and demonstrates a high level of consistency in the experimentally measured Young's modulus values in each of the sample sets. Similar trends are evident when observing the mean yield and compressive strength properties. Here, the 8-cell metamaterial exhibits the highest mean yield and compressive strength values at 4.90 MPa and 5.91 MPa, respectively. The yield strength value is 175% higher and the compressive strength is 150% higher when compared against the hexagonal honeycomb tested out-of-plane, which yields on average at 2.80 MPa and reaches a maximum compressive strength on average at 3.95 MPa. The 5-cell and 16-cell yield and compressive strengths surpass those of the gyroid, while the 24-cell

Table 4: Mean specific yield strength values $\left(\frac{\bar{\sigma}_y}{\rho}\right)$ results for experimental samples: 5, 8, 16 and 24-cell metamaterials, as well as gyroid and honeycomb structures, and specific strength values $\left(\frac{\sigma_y}{\rho}\right)$ for simulated models: 5, 8, 16 and 24-cell metamaterials.

Experimental	5-cell	8-cell	16-cell	24-cell	Gyroid	Hex honeycomb
Mean specific yield strength $\left(\frac{\bar{\sigma}_y}{\rho}\right)$ (kNm/kg)	12.62	22.80	7.16	6.28	5.72	19.43
Upper value	13.59	25.58	7.69	6.65	5.86	22.95
Lower value	10.62	19.32	6.72	5.53	5.46	16.96
Median	13.57	22.73	7.17	6.41	5.81	19.22
Standard deviation	1.226	2.046	0.383	0.417	0.152	2.032
CoV	9.7%	9.0%	5.4%	6.6%	2.7%	10.5%
Simulations						
Specific yield strength $\left(\frac{\sigma_y}{\rho}\right)$ (kNm/kg)	15.76	25.28	9.29	7.90	N/A	N/A
Percentage diff. (sim. vs exp.)	20.0%	9.8%	22.9%	20.5%	N/A	N/A
Z-score	2.56	1.21	5.57	3.89	N/A	N/A

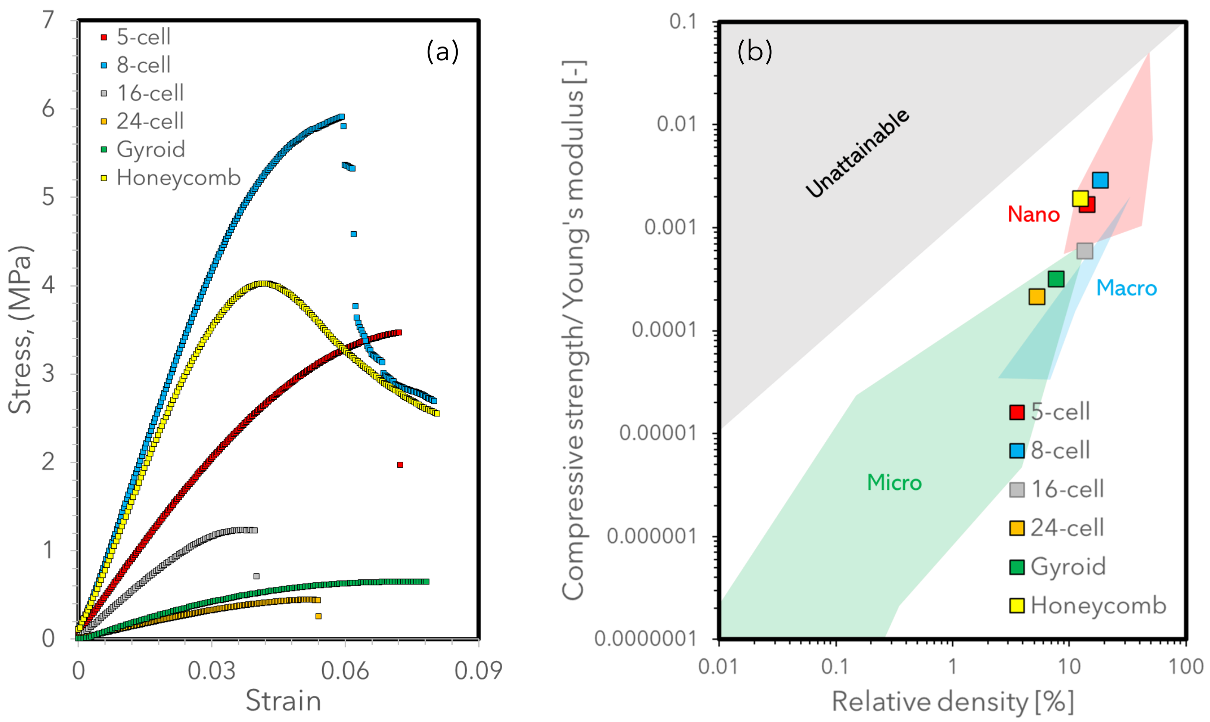

Figure 10: (a) Representative compressive stress-strain curves for each of the experimental sample sets (3D projected 4-polytopes, gyroids and hexagonal honeycombs), and (b) the compressive strength normalised by bulk Young's modulus plotted against the relative density of the sample - the data points are plotted against generalised area plots for different metamaterial structures at the nano, micro and macro length scales.

metamaterial, which also has the lowest apparent density, is the weakest of the six structures under scrutiny. The experimental data additionally suggests that the 8-cell followed by the 5-cell metamaterials, have a higher ability to absorb elastic energy when compared against the hexagonal honeycomb samples, outperforming the latter by 3.4 and 1.9 times, respectively. When compared to the 3-dimensional gyroid, all of the 4-polytope projected metamaterials exhibit a higher modulus of resilience, demonstrating the suitability of these structures in applications where elastic

Table 5: Summary of experimentally obtain mechanical properties: Young's modulus (compression), yield and compressive strength, modulus of resilience and modulus of toughness for 4-polytope projected metamaterials, and for gyroid and hexagonal honeycomb structures.

	5-cell	8-cell	16-cell	24-cell	Gyroid	Hex honeycomb
Young's modulus, (MPa)	70.53	145.01	43.52	11.73	15.30	128.75
SD	3.59	14.21	4.36	0.39	0.13	14.38
CoV	5.09%	9.80%	10.01%	3.37%	0.85%	11.17%
Yield strength, (MPa)	2.09	4.90	1.13	0.38	0.51	2.80
SD	0.20	0.44	0.06	0.03	0.01	0.29
CoV	9.72%	8.97%	5.35%	6.64%	2.66%	10.46%
Compressive strength, (MPa)	3.47	5.91	1.22	0.44	0.65	3.95
SD	0.28	0.56	0.05	0.01	0.01	0.44
CoV	8.14%	9.45%	3.79%	3.33%	1.04%	11.12%
Modulus of resilience, (kJ/m^3)	53.50	95.32	14.37	7.88	6.29	27.95
SD	12.30	11.97	2.44	1.01	1.09	4.40
CoV	22.99%	12.56%	17.02%	12.85%	17.26%	15.74%
Modulus of toughness, (kJ/m^3)	130.21	294.50	32.04	14.52	48.62	239.16
SD	14.48	32.71	7.57	1.43	10.50	37.43
CoV	11.12%	11.11%	23.62%	9.84%	21.60%	15.65%

Table 6: Apparent and relative densities of simulated and experimentally tested samples.

	Simulations		Experimental	
	Apparent density, (kg/m3)	Relative density	Apparent density, (kg/m3)	Relative density
5-cell	154.00	13.22%	165.54	14.21%
8-cell	199.48	17.12%	214.73	18.43%
16-cell	139.24	11.95%	157.59	13.53%
24-cell	54.65	4.69%	61.09	5.24%
Gyroid	N/A	N/A	89.02	7.64%
Honeycomb	N/A	N/A	144.02	12.36%

energy storage in compression is a key design consideration. Nevertheless, as compressive loading increases beyond the elastic limit, the 4-polytope projected metamaterials display a relatively short plastic region when compared to that of the honeycomb and gyroid structures. Moreover, the plastic regions of the 4-polytope projected metamaterials are coupled to catastrophic failure soon after reaching maximum compressive strength. As such, the 4-polytope projected metamaterials are significantly more brittle than the honeycomb and gyroid structures, which is in turn an artifact of an optimisation process that favoured elastic energy storage. It can therefore be inferred that maximising the elastic strain energy storage capacity of a metamaterial concurrently minimises its ability to gradually release energy through plastic deformation and as such, catastrophic failure is an expected mechanical behaviour that is borne through the optimisation process. Finally, the modulus of toughness is highest in the 8-cell metamaterial (294.50 kJ/m^3), followed by the hexagonal honeycomb (239.16 kJ/m^3). The 5-cell metamaterial fails at the strain of 0.074 and has a modulus of toughness of 130.21 kJ/m^3, which is higher 2.68 times higher than that for a gyroid over its complete 0.08 strain range. The toughness values for 16-cell and 24-cell metamaterials are significantly lower (32.04 and 14.52 kJ/m^3, respectively). This is ultimately a consequence of sample fracture at low strain values. The 16-cell metamaterials failed on average at a strain of 0.04, while the 24-cell metamaterials failed at an average strain of 0.055. In Figure 10 (b) the compressive strength normalised by the bulk Young's modulus of fully cured solid resin is plotted against the relative density of the sample provided in Table 6. This is a normalisation method by which means the strength gain of metamaterials can be visualised [48]. In this figure, the data points are plotted against generalised area plots for different metamaterial structures at the nano, micro and macro length scales, based on data from [48]. Honeycomb structures tested in the out-of-plane direction are generally expected to display a high normalised compressive strength at relatively low densities, and this is observed in Figure 10 (b), where the (macro-scale) honeycomb is at a level that is typically a lower level of nanostructures, which themselves ordinarily have normalised strengths above those of macro-structures. Noting this, it can also be observed that the (macro-scale) 8-cell metamaterials have higher normalised strength and relative density values than the honeycomb structures, while 5-cell metamaterials are similar to honeycombs. Contrarily, the gyroid and 24-cell metamaterials exhibit a notably lower normalised strength with respect to their relative densities, while the 16-cell metamaterials show fairly typical properties for generic macro-structures such as macrolattices.

Table 7: Calculations of constants C and D using experimental data in Tables 5 and 6.

	C	D
5-cell	0.30	0.25
8-cell	0.45	0.44
16-cell	0.20	0.14
24-cell	0.15	0.14
Gyroid	0.13	0.12
Honeycomb	0.65	0.39

As mentioned in Section 1, Choi and Lee [47] hypothesise that the strength and stiffness of strut-based hypercubes (i.e. strut-based tesseracts) can be represented as $\left(\frac{E*}{E_s}\right) = C\left(\frac{\rho*}{\rho_s}\right)^a$ and $\left(\frac{\sigma*}{\sigma_s}\right) = D\left(\frac{\rho*}{\rho_s}\right)^b$, and conclude that in hypercubes where the pore space is unfilled, $a = b = 1.11$ and $C = 0.023$ while $D = 0.01$. Taking the mean values of the Young's modulus and yield stress from Table 5 as inputs for $E*$ and $\sigma*$, the experimental relative densities from Table 6 as input values for $\frac{\rho*}{\rho_s}$, and and $a = b = 1.11$, the C and D constants are calculated and shown for each of the structures in Table 7. The C and D constants provide value as they allude to residual stiffness and strength, respectively, as reduced stiffnesses and strengths from a solid block of material due to the presence of pore space. There is a large difference between C and D for the honeycomb structures, which indicates that while these structures are superior in terms of stiffness ($C = 0.65$), they lose significant mechanical value when it comes to strength ($D = 0.39$), and this may be due to how honeycombs will buckle causing an onset of plastic straining, after which they crumble. 5-cell and 16-cell metamaterials also display notable differences between C and D constants however, these are not as extreme as in honeycomb structures. Both 8-cell and 24-cell metamaterials, as well as gyroids, retain relative closeness between their C and D constants, indicating that both strength and stiffness are equally reduced from the bulk material properties due to pore space. Nevertheless, the optimised 8-cell metamaterial structures have significantly higher C and D constants than have previously been reported [47] exceeding the previous constants for tesseracts by ca. 20-fold and 44-fold in terms of stiffness and strength, respectively. It should be nevertheless be noted that the properties of mechanical metamaterials are governed by architecture, length scale and material composition as affected by the manufacturing, in parallel [48]. As such, the comparisons made herein are primarily to showcase how 3D projected 4D geometries compare in terms of residual strength and stiffness as reduced through the presence of pore space. What we find here therefore, is that architecture has a profound effect on the relative consistency of properties. Cubically symmetric structures display the greatest levels of consistency in terms of both strength and stiffness reductions from the presence of unfilled, empty spaces (porosity), while of these, tesseract, octaplex and gyroid structures are the most consistent.

4. Conclusions

This paper proposes for the first time, the use of 3D projections of 4D geometries (4-polytopes) as a basis for metamaterial design and optimisation. Our research clearly demonstrates that this new class of mechanical metamaterial has considerable potential as cubically symmetrical structures with superior properties of specific stiffness and strength. While such structures have the obvious benefit of being enablers of multi-directional mechanical resistance, certain forms e.g. 8-cell (tesseract) and 24-cell (octaplex) structures, reduce equally from the original bulk properties in terms of strength and stiffness, with respect to pore-space. This characteristic is not seen in more common honeycomb structures, though it is evident in gyroids, most plausibly because the gyroids are also cubically symmetric. Genetic algorithms coupled with parametric optimisation have improved the properties of specific stiffness of 4-polytope projections by ca. 65%, 38%, 137% and 78% for 5-cell (pentatope), 8-cell (tesseract), 16-cell (orthoplex) and 24-cell (octaplex) metamaterials. Nevertheless, only certain structures amongst the optimised 4-polytope projections show significant promise in terms of their final properties. In particular, the optimised 8-cell tesseract has a higher specific yield strength than even hexagonal honeycomb structures loaded in the out-of-plane direction, and their specific stiffness values are within the same range of values measured for the honeycombs. Both the 8-cell tesseract as well as the 5-cell pentatope, in similitude to the honeycomb structures, have very high normalised compressive strengths and lie within the range of values for nanolattice based metamaterials when plotted against their relative densities, the 8-cell tesseract being the highest of the three aforementioned structures. The optimisation methodology and corresponding results evidence that there is validity and significance in developing advanced mechanical metamaterials from 3D projections of 4-polytopes. The parametric design approach in combination with evolutionary algorithm based optimisation used herein, demonstrates that mechanical performance can be enhanced whilst maintaining lightweightness. The cubically symmetrical nature of 4-polytope projections offers great advantages for maintaining structural stiffness for multi-axial loading, which is beneficial in many real-life applications. As shown herein, the proposed design framework can also be used to optimise other mechanical properties besides the properties of specific stiffness and strength.

5. Data Availability

Data for this paper will be available on the Edinburgh Data Share website (https://datashare.ed.ac.uk/).

Author Contributions

Conceptualisation (PA); Data curation (GC and PA); Formal analysis (GC and PA); Funding acquisition (PA); Investigation (GC); Methodology (GC and PA); Project administration (GC and PA); Resources (GC and PA); Software (GC); Supervision (PA); Validation (GC and PA); Visualisation (GC and PA); Roles/Writing - original draft (GC); Writing - review and editing (PA).

References

[1] P. U. Kelkar, H. S. Kim, K. H. Cho, J. Y. Kwak, C. Y. Kang, H. C. Song, Cellular Auxetic Structures for Mechanical Metamaterials: A Review, Sensors 2020, Vol. 20, Page 3132 20 (11) (2020) 3132. doi:10.3390/S20113132.
URL https://www.mdpi.com/1424-8220/20/11/3132/htmhttps://www.mdpi.com/1424-8220/20/11/3132

[2] S. Babaee, J. Shim, J. C. Weaver, E. R. Chen, N. Patel, K. Bertoldi, 3D Soft Metamaterials with Negative Poisson's Ratio, Advanced Materials 25 (36) (2013) 5044–5049. doi:10.1002/ADMA.201301986.
URL https://onlinelibrary.wiley.com/doi/full/10.1002/adma.201301986https://onlinelibrary.wiley.com/doi/abs/10.1002/adma.201301986https://onlinelibrary.wiley.com/doi/10.1002/adma.201301986

[3] J. Gao, H. Xue, L. Gao, Z. Luo, Topology optimization for auxetic metamaterials based on isogeometric analysis, Computer Methods in Applied Mechanics and Engineering 352 (2019) 211–236. doi:10.1016/J.CMA.2019.04.021.

[4] A. L. Ruschel, A. F. Samuel, M. C. Martinez, M. R. Begley, F. W. Zok, A 3D bi-material lattice concept for tailoring compressive properties, Materials and Design 224 (12 2022). doi:10.1016/J.MATDES.2022.111265.

[5] M. Ye, L. Gao, H. Li, A design framework for gradually stiffer mechanical metamaterial induced by negative Poisson's ratio property, Materials and Design 192 (7 2020). doi:10.1016/J.MATDES.2020.108751.

[6] S. Yuan, C. Kai Chua, K. Zhou, S. Yuan, C. K. Chua, K. Zhou, 3D-Printed Mechanical Metamaterials with High Energy Absorption, Advanced Materials Technologies 4 (3) (2019) 1800419. doi:10.1002/ADMT.201800419.
URL https://onlinelibrary.wiley.com/doi/full/10.1002/admt.201800419https://onlinelibrary.wiley.com/doi/abs/10.1002/admt.201800419https://onlinelibrary.wiley.com/doi/10.1002/admt.201800419

[7] W. Yang, S. Dong, X. Zhu, S. Ren, L. Li, Superior energy absorption performance of layered aux-hex honeycomb filled tubes, International Journal of Mechanical Sciences 234 (March) (2022) 107702. doi:10.1016/j.ijmecsci.2022.107702.
URL https://doi.org/10.1016/j.ijmecsci.2022.107702

[8] J. B. Berger, H. N. Wadley, R. M. McMeeking, Mechanical metamaterials at the theoretical limit of isotropic elastic stiffness, Nature 2016 543:7646 543 (7646) (2017) 533–537. doi:10.1038/nature21075.
URL https://www.nature.com/articles/nature21075

[9] M. Hashemi, A. McCrary, K. Kraus, A. Sheidaei, A novel design of printable tunable stiffness metamaterial for bone healing, Journal of the Mechanical Behavior of Biomedical Materials 116 (2021). doi:10.1016/j.jmbbm.2021.104345.

[10] W. Lee, D. Y. Kang, J. Song, J. H. Moon, D. Kim, Controlled Unusual Stiffness of Mechanical Metamaterials, Scientific Reports 2016 6:1 6 (1) (2016) 1–7. doi:10.1038/srep20312.
URL https://www.nature.com/articles/srep20312

[11] X. Yu, J. Zhou, H. Liang, Z. Jiang, L. Wu, Mechanical metamaterials associated with stiffness, rigidity and compressibility: A brief review, Progress in Materials Science 94 (2018) 114–173. doi:10.1016/J.PMATSCI.2017.12.003.

[12] P. Jiao, A. Alavi, Artificial intelligence-enabled smart mechanical metamaterials: advent and future trends, International Materials Reviews (2020). doi:10.1080/09506608.2020.1815394.

[13] S. Katoch, S. S. Chauhan, V. Kumar, A review on genetic algorithm: past, present, and future, Multimedia Tools and Applications 80 (5) (2021) 8091–8126. doi:10.1007/S11042-020-10139-6/FIGURES/8.
URL https://link.springer.com/article/10.1007/s11042-020-10139-6

[14] C. Wang, X. Tan, S. Tor, C. Lim, Machine learning in additive manufacturing: State-of-the-art and perspectives, Additive Manufacturing 36 (2020). doi:10.1016/j.addma.2020.101538.

[15] S. Bonfanti, R. Guerra, M. Zaiser, S. Zapperi, Digital strategies for structured and architected materials design, APL Materials 9 (2) (2021). doi:10.1063/5.0026817.

[16] I. Zhilyaev, D. Krushinsky, M. Ranjbar, A. O. Krushynska, Hybrid machine-learning and finite-element design for flexible metamaterial wings, Materials & Design 218 (2022) 110709. doi:10.1016/J.MATDES.2022.110709.

[17] N. Changizi, G. P. Warn, Topology optimization of structural frames considering material nonlinearity and time-varying excitation, Structural and Multidisciplinary Optimization (4 2021). doi:10.1007/s00158-020-02776-0.

[18] A. Bacigalupo, G. Gnecco, M. Lepidi, L. Gambarotta, Design of acoustic metamaterials through nonlinear programming, in: Lecture Notes in Computer Science (including subseries Lecture Notes in Artificial Intelligence and Lecture Notes in Bioinformatics), Vol. 10122 LNCS, Springer Verlag, 2016, pp. 170–181. doi:10.1007/978-3-319-51469-7{_}14.

[19] R.-B. Yang, J. Yang, S. Lo, Wideband square spiral metamaterial absorbers based on flaky carbonyl iron/epoxy composites, AIP Advances 10 (1) (2020). doi:10.1063/1.5130470.

[20] L. Singleton, J. Cheer, S. Daley, Design of a resonator-based metamaterial for broadband control of transverse cable vibration, in: Proceedings of the International Congress on Acoustics, Vol. 2019-September, International Commission for Acoustics (ICA), 2019, pp. 5589–5596. doi:10.18154/RWTH-CONV-239432.

[21] M. Mansouree, A. Arbabi, Metasurface Design Using Level-Set and Gradient Descent Optimization Techniques, in: 2019 International Applied Computational Electromagnetics Society Symposium in Miami, ACES-Miami 2019, Institute of Electrical and Electronics Engineers Inc., 2019.

[22] H. M. Sheikh, T. Meier, B. Blankenship, Z. Vangelatos, N. Zhao, P. S. Marcus, C. P. Grigoropoulos, Systematic design of Cauchy symmetric structures through Bayesian optimization, International Journal of Mechanical Sciences (2022) 107741doi:10.1016/J.IJMECSCI.2022.107741.

[23] C. Sharpe, C. C. Seepersad, S. Watts, D. Tortorelli, Design of Mechanical Metamaterials via Constrained Bayesian Optimization, Proceedings of the ASME Design Engineering Technical Conference 2A-2018 (11 2018). doi:10.1115/DETC2018-85270.

[24] W. Jiang, Y. Zhu, G. Yin, H. Lu, L. Xie, M. Yin, Dispersion relation prediction and structure inverse design of elastic metamaterials via deep learning, Materials Today Physics 22 (1 2022). doi:10.1016/J.MTPHYS.2022.100616.

[25] H. Kollmann, D. Abueidda, S. Koric, E. Guleryuz, N. Sobh, Deep learning for topology optimization of 2D metamaterials, Materials and Design 196 (2020). doi:10.1016/j.matdes.2020.109098.

[26] H. Meng, D. Chronopoulos, A. Fabro, I. Maskery, Y. Chen, Optimal design of rainbow elastic metamaterials, International Journal of Mechanical Sciences 165 (2020). doi:10.1016/j.ijmecsci.2019.105185.

[27] L. Wang, H.-T. Liu, Parameter optimization of bidirectional re-entrant auxetic honeycomb metamaterial based on genetic algorithm, Composite Structures 267 (2021). doi:10.1016/j.compstruct.2021.113915.

[28] Y. Chen, J. Yan, J. Feng, P. Sareh, Particle Swarm Optimization-Based Metaheuristic Design Generation of Non-Trivial Flat-Foldable Origami Tessellations with Degree-4 Vertices, Journal of Mechanical Design, Transactions of the ASME 143 (1) (2021). doi:10.1115/1.4047437.

[29] K. Qiu, R. Wang, Z. Xie, J. Zhu, W. Zhang, Optimal design of chiral metamaterials with prescribed nonlinear properties, Structural and Multidisciplinary Optimization (2020). doi:10.1007/s00158-020-02747-5.

[30] R. Ghachi, W. Alnahhal, O. Abdeljaber, J. Renno, A. Tahidul Haque, J. Shim, A. Aref, Optimization of Viscoelastic Metamaterials for Vibration Attenuation Properties, International Journal of Applied Mechanics 12 (10) (2020). doi:10.1142/S1758825120501161.

[31] W. Sha, M. Xiao, M. Huang, L. Gao, Topology-optimized freeform thermal metamaterials for omnidirectionally cloaking sensors, Materials Today Physics 28 (2022) 100880. doi:10.1016/J.MTPHYS.2022.100880.

[32] M. Ye, L. Gao, F. Wang, H. Li, A novel design method for energy absorption property of chiral mechanical metamaterials, Materials 14 (18) (2021) 1–21. doi:10.3390/ma14185386.

[33] J. Dong, C. Hu, J. Holmes, Q. H. Qin, Y. Xiao, Structural optimisation of cross-chiral metamaterial structures via genetic algorithm, Composite Structures 282 (2022) 115035. doi:10.1016/J.COMPSTRUCT.2021.115035.

[34] D. Wang, L. Dong, G. Gu, D. Wang, L. Dong, G. Gu, 3D Printed Fractal Metamaterials with Tunable Mechanical Properties and Shape Reconfiguration, Advanced Functional Materials (2022) 2208849doi:10.1002/ADFM.202208849.
URL https://onlinelibrary.wiley.com/doi/full/10.1002/adfm.202208849https://onlinelibrary.wiley.com/doi/abs/10.1002/adfm.202208849https://onlinelibrary.wiley.com/doi/10.1002/adfm.202208849

[35] Z. Yang, P. Alam, Designing Hierarchical Honeycombs to Mimic the Mechanical Behaviour of Composites, Journal of Composites Science 2021, Vol. 5, Page 17 5 (1) (2021) 17. doi:10.3390/JCS5010017.
URL https://www.mdpi.com/2504-477X/5/1/17/htmhttps://www.mdpi.com/2504-477X/5/1/17

[36] C. C. Vu, T. T. N. Truong, J. Kim, Fractal structures in flexible electronic devices, Materials Today Physics 27 (2022) 100795. doi:10.1016/J.MTPHYS.2022.100795.

[37] R. S. Farr, Y. Mao, Fractal space frames and metamaterials for high mechanical efficiency, EPL 84 (2008) 14001. doi:10.1209/0295-5075/84/14001.
URL www.epljournal.org

[38] D. Rayneau-Kirkhope, Y. Mao, R. Farr, Ultralight fractal structures from hollow tubes, Physical Review Letters 109 (20) (2012) 204301. doi:10.1103/PHYSREVLETT.109.204301/FIGURES/4/MEDIUM.
URL https://journals.aps.org/prl/abstract/10.1103/PhysRevLett.109.204301

[39] D. Celento, E. Harriss, Potentials for Multi-dimensional Tessellations in Architectural Applications.

[40] J. Constant, The Octaplex, Symmetry in Four-Dimensional Geometry and Art, Materials Today: Proceedings 5 (8) (2018) 15935–15942. doi:10.1016/J.MATPR.2018.06.066.

[41] K. Miyazaki, I. Takada, H. Nakata, Geometrical Beauty in Four-Dimensional Space, Katachi âª Symmetry (1996) 215–222doi:10.1007/978-4-431-68407-7{_}23.
URL https://link.springer.com/chapter/10.1007/978-4-431-68407-7_23

[42] M. Petrov, T. Todorov, G. Walters, D. William, F. Witherden, Enabling four-dimensional conformal hybrid meshing with cubic pyramids, Numerical Algorithms (2022) 671–709doi:10.1007/s11075-022-01278-y.
URL https://link.springer.com/article/10.1007/s11075-022-01278-y

[43] M. Petrov, T. Todorov, Properties of Multipyramidal Elements, Computational Science and Its Applications â ICCSA 2021. ICCSA 2021. Lecture Notes in Computer Science (2021) 12949doi:10.1007/978-3-030-86653-2_40.
URL https://link.springer.com/chapter/10.1007/978-3-030-86653-2_40

[44] M. Petrov, T. Todorov, An Algorithm for Polytope Overlapping Detection, Computational Science and Its Applications â ICCSA 2021. ICCSA 2021. Lecture Notes in Computer Science (2021) 12949doi:10.1007/978-3-030-86653-2_2.
URL https://doi.org/10.1007/978-3-030-86653-2_2

[45] M. Petrov, T. Todorov, Stable subdivision of 4D polytopes, Numerical Algorithms (2018) 633–656doi:10.1007/s11075-017-0454-2.
URL https://link.springer.com/article/10.1007/s11075-017-0454-2

[46] R. Naboni, A. Kunic, Trabecular Tectonics. 3D Printed Cellular Structures for Architectural Applications, Gestao e Tecnologia de Projetos (2019) 111–124doi:10.11606/gtp.v14i1.148496.
URL http://dx.doi.org/10.11606/gtp.v14i1.148496

[47] J. Choi, S.-i. Lee, Experimental validation of theoretical models for hypercube models made by fused deposition modelling technology, Journal of Mechanical Science and Technology (2019) 5951–5961doi:10.1007/s12206-019-1140-1.
URL https://link.springer.com/content/pdf/10.1007/s12206-019-1140-1.pdf

[48] J. Bauer, L. R. Meza, T. A. Schaedler, R. Schwaiger, X. Zheng, L. Valdevit, Nanolattices: An Emerging Class of Mechanical Metamaterials, Advanced Materials 29 (2017) 1701850. doi:10.1002/adma.201701850.
URL https://onlinelibrary.wiley.com/doi/10.1002/adma.201701850